Accepted for publication in the Astrophysical Journal Letters, July 21, 2015
Preprint typeset using LaTeX style emulateapj v. 01/23/15

WHY HAVEN'T MANY OF THE BRIGHTEST RADIO LOUD BLAZARS BEEN DETECTED IN GAMMA-RAYS BY *FERMI* ?

M. L. Lister[1], M. F. Aller[2], H. D. Aller[2], T. Hovatta[3,4], W. Max-Morbeck[5], A. C. S. Readhead[4], J. L. Richards[1], E. Ros[6,7,8]

Accepted for publication in the Astrophysical Journal Letters, July 21, 2015

ABSTRACT

We use the complete MOJAVE 1.5 Jy sample of active galactic nuclei (AGN) to examine the gamma-ray detection statistics of the brightest radio-loud blazars in the northern sky. We find that 23% of these AGN were not detected above 0.1 GeV by the *Fermi* LAT during the 4-year 3FGL catalog period partly because of an instrumental selection effect, and partly due to their lower Doppler boosting factors. Blazars with synchrotron peaks in their spectral energy distributions located below $10^{13.4}$ Hz also tend to have high-energy peaks that lie below the 0.1 GeV threshold of the LAT, and are thus less likely to be detected by *Fermi*. The non-detected AGN in the 1.5 Jy sample also have significantly lower 15 GHz radio modulation indices and apparent jet speeds, indicating that they have lower than average Doppler factors. Since the effective amount of relativistic Doppler boosting is enhanced in gamma-rays (particularly in the case of external inverse-Compton scattering), this makes them less likely to appear in the 3FGL catalog. Based on their observed properties, we have identified several bright radio-selected blazars that are strong candidates for future detection by *Fermi*.

Keywords: galaxies: active — galaxies: jets — quasars: general — radio continuum: galaxies — gamma rays: galaxies

1. INTRODUCTION

The *Fermi* space telescope is a powerful broad-band gamma-ray facility that has continuously scanned the entire sky every 3 hours since 2008. One of its major discoveries has been that away from the galactic plane, the gamma-ray sky is dominated by the blazar class of active galactic nuclei (AGN) (Abdo et al. 2010a). These relatively rare AGN harbor powerful jets of relativistically-moving plasma that are oriented close to our line of sight. Their overall spectral energy distribution (SED) tends to be dominated by relativistically boosted emission from the jet, and typically consists of two broad peaks in a plot of log νF_ν versus log ν, where F_ν is the observed flux density at frequency ν (Abdo et al. 2010e). The lower frequency peak is associated with synchrotron emission from relativistic electrons in the jet plasma, while the high frequency peak is widely believed to be created by inverse-Compton (IC) up-scattering of photons from the jet, accretion disk and/or broad line region (e.g., Dermer & Schlickeiser 1993; Sikora et al. 1994).

Since the same population of jet electrons is responsible for these two peaks, we might expect the synchrotron and gamma-ray emission from individual blazars to be correlated, and this has proven to be the case. Many studies have found statistical correlations between the radio/sub-mm band and the > 0.1 GeV time-averaged fluxes measured by the *Fermi* LAT instrument (e.g., Kovalev et al. 2009; Ackermann et al. 2011; Lister et al. 2011; Giommi et al. 2012; Fuhrmann et al. 2014; Mufakharov et al. 2015). Mahony et al. (2010) have also shown that the fraction of radio-loud AGN detected by *Fermi* steadily increases with increasing 20 GHz flux density.

Despite these well-established correlations, it is still not fully understood why a substantial fraction of the brightest, most compact blazars in the GHz band have not been detected at energies above 0.1 GeV, despite the four years of continuous observations included in the most recent *Fermi* catalog (3FGL; Acero et al. 2015). In this *Letter*, we investigate the properties of a complete flux density-limited, 15 GHz AGN sample of the northern sky, the MOJAVE 1.5 Jy survey, where 23% of the AGN have no *Fermi* detections. We show that these non-detected AGN have a lower than average jet speed and radio variability index (indicative of a lower Doppler boosting factor) and a synchrotron component that peaks below $\sim 10^{13.4}$ Hz. The latter causes their secondary SED peak to be located well below the lower energy cutoff of the LAT instrument, resulting in a low LAT gamma-ray flux and non-detection by *Fermi*. We discuss the 1.5 Jy sample and observational data in § 2, present our analysis in § 3, and summarize our conclusions in § 4.

[1] Department of Physics, Purdue University, 525 Northwestern Avenue, West Lafayette, IN 47907, USA; mlister@purdue.edu
[2] Department of Astronomy, University of Michigan, 311 West Hall, 1085 S. University Avenue, Ann Arbor, MI 48109, USA;
[3] Aalto University, Metsähovi Radio Observatory, Metsähovintie 114, FI-02540, Kylmälä, Finland;
[4] Cahill Center for Astronomy & Astrophysics, California Institute of Technology, 1200 E. California Blvd, Pasadena, CA 91125, USA;
[5] National Radio Astronomy Observatory, P.O. Box O 1003 Lopezville Road Socorro, NM 87801-038, USA;
[6] Max-Planck-Institut für Radioastronomie, Auf dem Hügel 69, 53121 Bonn, Germany
[7] Observatori Astronòmic, Universitat de València, Parc Científic, C. Catedrático José Beltrán 2, E-46980 Paterna, València, Spain;
[8] Departament d'Astronomia i Astrofísica, Universitat de València, C. Dr. Moliner 50, E-46100 Burjassot, València, Spain;

2. OBSERVATIONAL DATA

In order to properly evaluate the statistics of gamma-ray detections of bright radio loud blazars, it is essential to use well-defined, complete samples. The GeV and radio bands above $\sim$ 10 GHz are ideal in this respect due to the lack of foreground obscuration (away from the galactic plane), and little contamination from non-active galaxies. In these bands, the AGN emission is dominated by that of the jet, with little contribution from the extended lobes. In this section we describe the radio-selected MOJAVE 1.5 Jy AGN sample, and the supporting data from our own studies and the literature.

2.1. *Radio data*

In the GHz band, there have been many large sky surveys carried out over the last few decades, e.g., FIRST (Becker et al. 1995), NVSS (Condon et al. 1998), GB6 (Gregory et al. 1996), AT20G (Murphy et al. 2010), such that virtually every radio loud AGN above 1 Jy has been identified and cataloged. Nevertheless, a major challenge in obtaining complete samples of radio loud blazars has been their highly variable flux densities, which over the course of several years can change by factors exceeding ~ 10 in the GHz band (Richards et al. 2014), and ~ 200 in the GeV band (Abdo et al. 2010c; Fuhrmann et al. 2014). Any single epoch flux-limited survey therefore stands to miss a substantial portion of the population.

As part of a VLBA key project to study the parsec-scale structure and evolution of AGN jets (Lister et al. 2009b), we have constructed a complete, flux density-limited sample, based on all available GHz band flux density data on bright radio AGNs over a 16 year period from 1994.0 to 2010.0 (Lister et al. 2013). The MOJAVE 1.5 Jy sample includes all AGN (excluding gravitational lenses) located north of J2000 declination -30° that are known to have exceeded 1.5 Jy in compact (milliarcsecond-scale) 15 GHz flux density at least once during that period. We were able to estimate the milliarcsecond-scale flux density from single-dish measurements by using near-simultaneous VLBA/single-dish observations of each source at several epochs. The difference of these near-simultaneous measurements represents the amount of arcsecond-scale emission resolved out by the VLBA, which is expected to be non-variable due to its size. Given the measurement errors, we were able to detect any extended emission above 0.02 Jy.

Using newly obtained data from the OVRO 15 GHz AGN monitoring program (Richards et al. 2011), we have refined our extended flux density estimates and subsequently dropped two AGN (MG1 J021114+1051 and OP -050) from the original 1.5 Jy sample list. We list the properties of all 181 AGN in the revised sample in Table 1. For the purposes of this paper, we consider only the 163 AGN that are located at least 10 degrees away from the galactic plane. This ensures that issues related to galactic gamma-ray foreground subtraction do not affect the LAT detection statistics of our sample.

2.2. *Gamma-ray data*

The Third *Fermi* Gamma-Ray Catalog (3FGL; Acero et al. 2015) is based on LAT data collected between 2008 August 4 and 2012 July 31, and contains 3033 high-confidence detections above 0.1 GeV. The Third LAT AGN Catalog (3LAC; Ackermann et al. 2015), associates 1563 of these sources with AGN. Because of the relatively large sky position errors ($\sim$ several arcmin) of the 3FGL sources, true counterpart identification has only been achieved in 12% of the cases. The remainder of the 3FGL associations were established using extensive statistical likelihood tests and a variety of celestial source catalogs. The 3LAC list consists of only high-confidence 3FGL AGN associations. For brevity, we will refer to these AGN as "LAT-detected" throughout this paper. Although a large number (992) of 3FGL gamma-ray sources remain unassociated, virtually all of the brightest ones have associations (see, e.g., Acero et al. 2015; Lister et al. 2011).

A total of 122 AGN in our sample are listed as associations in the 3LAC. Additionally, PKS 0539$-$057 and 4C + 06.69 appeared in the 1FGL catalog (Abdo et al. 2010a), and the LAT detection of 3C 120 was announced by Abdo et al. (2010b). The latter three AGN likely do not appear in the 3FGL catalog since they experienced at most only a brief period of gamma-ray flaring; thus their 4 year averaged fluxes were below the 3FGL significance cutoff. We checked the remaining non-LAT detected AGN in our sample, and in all cases the closest 3FGL source was at least 17 arcminutes away. There are also no *Fermi* associations for any of these AGN in the refined list published by Massaro et al. (2015).

2.3. *SED peak data*

As discussed previously by Finke (2013) there are considerable inconsistencies in the SED synchrotron peak locations of blazars reported in the literature. Since the peaks for most of our sample lie between 10^{12} and 10^{14} Hz, where there is typically a paucity of observational data, considerable interpolation-based errors are present. Since our AGN are highly core-dominated, any contribution from extended lobe emission to the SED is negligible above $\sim 10^{10}$ Hz, however, some authors have included the (non-jet) IR and optical big blue bump components in their polynomial fits to the synchrotron SED component, resulting in overestimates of the true peak location.

In order to minimize these errors, we have used the ASDC SED builder Version 3.1.6 tool[9] to estimate the peak location using a 3rd degree polynomial fit to flux densities published in the literature. For most of the AGN in our sample there were hundreds of available measurements at numerous frequencies, however, we only considered data up to 10^{14} Hz, and extended this up to 10^{15} Hz only for clear cases where the SED remained parabolic and there was no significant blue bump component. In some instances, there were insufficient flux density data or too much confusion from non-jet emission in the $10^{11.5}$ to 10^{14} Hz region to reliably estimate the location of the synchrotron peak. Based on comparisons to other published values in the literature for our AGN, we estimate a typical error of ± 0.3 dex in our values.

3. DISCUSSION

3.1. *Fermi detection and synchrotron peak location*

The passband of the LAT instrument covers photon energies in the approximate range of 100 MeV to 300 GeV

[9] https://tools.asdc.asi.it/

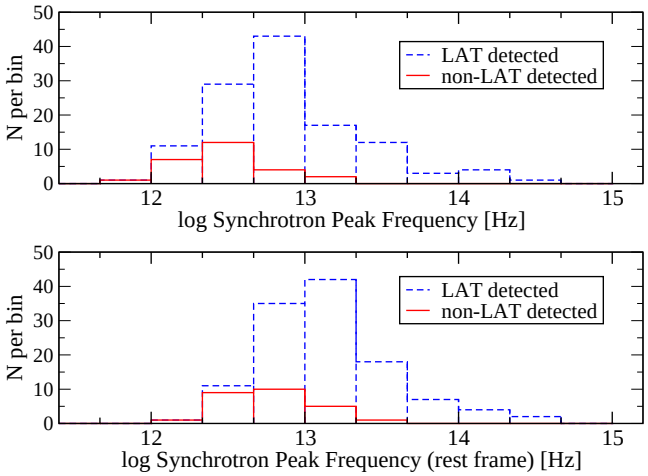

Figure 1. Top panel: distributions of observed synchrotron peak frequency for LAT detected (blue dashed line) and non-LAT detected (red solid line) sub-samples. Lower panel: same, but for rest frame synchrotron peak frequency.

(Atwood et al. 2009). At the highest energies, AGN detections are typically limited by low photon fluxes, since they typically have steep gamma-ray spectra with power law energy indices ranging from -1.5 to -3 (Acero et al. 2015). The LAT's fixed passband tends to discriminate against AGN with IC peaks located below 1 GeV, and those with very steep gamma-ray spectra. If the IC peak shapes of blazars are similar, then the LAT's fixed passband should create a correlation between the LAT energy index and the IC peak location. Unfortunately the latter are often difficult to measure, due to a lack of observational data in the soft gamma-ray and hard X-ray bands. However, we would also expect the locations of the synchrotron and IC peaks to be correlated, since the same population of jet electrons is responsible for both features. This has been shown to be the case, in the form of a relatively tight correlation between LAT energy index and synchrotron peak location (Abdo et al. 2010d). Therefore, since the two SED peaks track each other, AGN with low synchrotron peak locations should have IC peaks located well below the LAT bandpass, and consequently a smaller chance of detection by *Fermi*.

In Figure 1 we show histograms of synchrotron peak frequency for the LAT and non-LAT detected subsamples. All of the non-detected AGN have synchrotron peak frequencies below $10^{13.4}$ Hz (in both rest and observer frames). We performed two commonly-used nonparametric statistical tests to look for differences in the distributions. The Kolmogorov-Smirnov test evaluates possible differences in the cumulative distribution functions, while the Wilcoxon rank-sum test evaluates whether the data points of one sample are generally higher-valued (or lower-valued) than the other. We list the test results in Table 2. The LAT and non-LAT AGN have significantly different synchrotron peak distributions, both in the observed and rest frames. Figure 2 shows that as predicted, the AGN in our sample with higher synchrotron peak frequencies are more likely to be detected by *Fermi*.

3.2. *Fermi detection and Doppler boosting Indicators*

A main prediction of the external seed photon model for high-energy blazar emission is that the IC radiation should be more highly Doppler boosted than the synchrotron emission, due to a blue-shifting of the external photons in the rest frame of the jet electrons (Dermer 1995). The gamma-rays will also experience more effective boosting (via a k-correction) since their emission spectrum is much steeper than that of the flat-spectrum radio jet. There is already ample evidence that *Fermi* preferentially detects highly Doppler boosted jets; the very small number of misaligned (low Doppler factor) jets in the 3LAC (only 2% of the catalog) is a prime example. Other studies showing this *Fermi* selection bias include those by Kovalev et al. (2009), Abdo et al. (2010d), and Savolainen et al. (2010).

The Doppler factors of AGN jets are difficult to measure accurately, due to the featureless power-law nature of the jet emission, and a lack of a good means with which to estimate the jet viewing angle. Some studies (e.g., Lähteenmäki & Valtaoja 1999; Jorstad et al. 2005; Hovatta et al. 2009) have used light-crossing time arguments and variability timescales of individual flares to derive Doppler factors, but only for a relatively small number of AGN. However, the overall variability level of a blazar is also a good indicator of its Doppler factor, since any intrinsic variability will be significantly shortened and increased in amplitude by Doppler boosting (e.g., Lister 2001). The OVRO monitoring program has published 15 GHz modulation indices for nearly 1500 blazars, covering the time period 2008 January 1 to 2011 December 31. These indices are estimates of the standard deviation of the flux density of a source divided by its mean (Richards et al. 2011).

The gamma-ray detected AGN in the OVRO sample are significantly more radio variable than the non-detected ones (Richards et al. 2014), and we find this same trend for the 142 OVRO AGN in our sample. Richards et al. (2014) also found the level of AGN radio variability to *decrease* with increasing synchrotron peak frequency, but their sample includes significant numbers of AGN with observed synchrotron peaks above 10^{14} Hz, whereas there are only 4 such AGN in our sample.

Another method of estimating the amount of relativistic boosting comes from measurements of apparent jet speeds. Although it is possible for a jet to have a low apparent speed if it is aligned exceedingly close to the line of sight (i.e., a viewing angle $< 1/\Gamma$, where Γ is the bulk Lorentz factor), for large flux-limited jet samples the apparent speed will on average be well-correlated with Lorentz factor (Lister et al. 2001). The MOJAVE program has published maximum apparent jet speeds for 133 AGNs in our sample (Lister et al. 2013), and is currently obtaining multi-epoch VLBA data on the remainder.

In an earlier study using the first three months of *Fermi* data, we showed that the gamma-ray detected AGN in the original MOJAVE sample had higher apparent jet speeds (Lister et al. 2009a). This is also the case for our 1.5 Jy sample, at an even higher level of statistical confidence (Table 2). Taken together with the trend in modulation index, this indicates that the Doppler factor also plays an important role in determining which radio-loud blazars will be detected by *Fermi*.

3.3. *Fermi detection and other jet properties*

In addition to Doppler factor and synchrotron peak location, there are potentially other properties that can

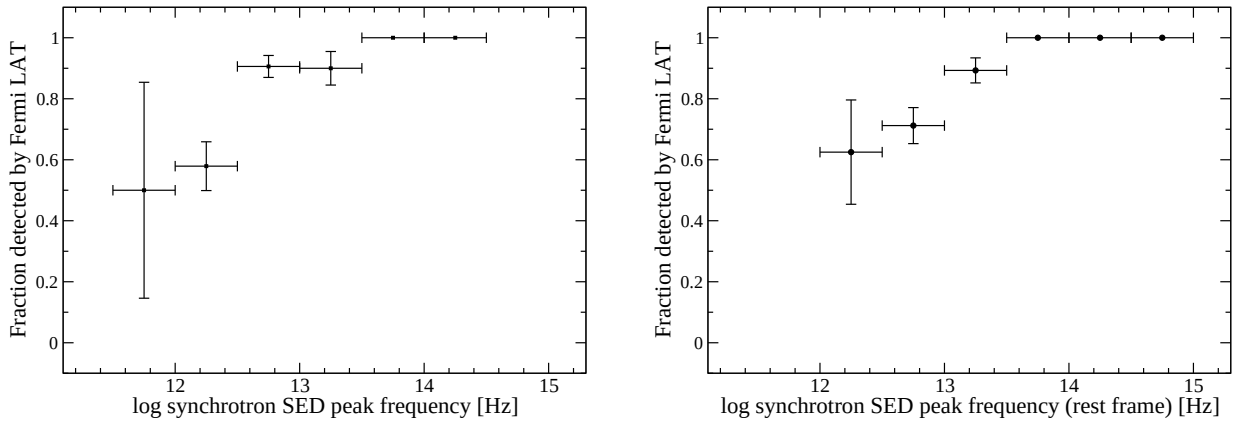

Figure 2. Left panel: LAT detection fraction versus synchrotron peak frequency. The vertical error bar for each bin assumes a binomial distribution with variance equal to $N \times f \times (f-1)$, where N is the number of AGN in the bin and f is the LAT detection fraction. Right panel: same, but for rest frame peak frequency.

also influence the gamma-ray flux of a blazar. These include redshift, intrinsic jet luminosity, and the activity state of the jet during the 3FGL observation period. The latter is particularly important when considering the *Fermi* detection statistics of the 1.5 Jy sample, which was selected over a time period that only partially overlaps that of the 3FGL catalog.

We have compiled maximum and median 15 GHz VLBA flux densities of the 1.5 Jy AGN during two time periods: a) between the start of the 1.5 Jy sample selection window (1994 January 1) and the start of *Fermi* operations (2008 August 4), and b) during the 3FGL observation window. We use the ratio of the maximum flux density in these two periods as a *Fermi*-era radio activity indicator, as was done by Kovalev et al. (2009) in their analysis of the *Fermi* LBAS list (Abdo et al. 2009). There were 51 AGN with insufficiently sampled flux density data in the pre-*Fermi* era to determine a reliable activity index.

The OVRO program does not include any AGN below declination $-20°$, and ten other 1.5 Jy sample AGN were only added to its monitoring list after the end of the 3FGL period. In all of these cases we had at least 4 epochs of VLBA[10] or UMRAO 14.5 GHz (Aller et al. 2014) observations during the 3FGL period with which to calculate maximum and median values.

We find no statistically significant differences in the activity indices of the LAT and non-LAT sub-samples. This is also the case for the median radio flux density during the 3FGL time period. There is a mild indication that the maximum radio flux densities of the LAT-detected AGN are higher on average than the non-detected ones. This is likely because the majority of the LAT detected AGN are highly variable in gamma-rays, and were detectable by *Fermi* only during a small fraction of the 3FGL time window (Acero et al. 2015).

There is no significant dependence of AGN LAT detection on redshift, maximum 3FGL-era radio luminosity, or median 3FGL-era radio luminosity. Our sample, being selected on radio jet emission, is dominated by high-luminosity, high-redshift jets, and contains only 11 AGN located closer than redshift 0.1. Consequently, it does not uniformly sample a wide range of jet luminosity, and is not ideally suited for probing the gamma-ray detection statistics of lower luminosity AGN.

[10] http://www.astro.purdue.edu/MOJAVE

4. SUMMARY AND CONCLUSIONS

We have examined the *Fermi* LAT detection statistics during the time period covered by the 3FGL catalog (2008 August 4 to 2012 July 31) of the MOJAVE 1.5 Jy complete flux density-limited sample of radio-loud blazars with J2000 declination $> -30°$ and $|b| > 10°$. We conclude that 23% of these AGN were not detected above 0.1 GeV by the *Fermi* LAT in part due to an instrumental selection effect, and partly due to lower relativistic boosting of their jet emission.

The LAT-detected blazars have significantly higher radio variability levels and apparent jet speeds than the non-detected ones. Both of these properties are positively correlated with the Doppler boosting factor of the radio emission. Since the effective amount of relativistic flux boosting is enhanced in gamma-rays (especially in the case of the external IC model), radio-selected blazars with lower than average Doppler factors are less likely to be detected by *Fermi*. In Figure 3, we plot apparent jet speed and modulation index, respectively, versus the rest frame synchrotron peak frequency. In both scatterplots there is a clear tendency for the non-LAT detected AGN to cluster in the lower left corner. In Figure 3 we have identified three AGN (III Zw 2, PKS 0119+11, and 4C +69.21), which based on their locations in the plots, are likely candidates for future LAT detection. The LAT's selection effects are clearly evident in the differences in the SED synchrotron peak locations of the detected and non-detected blazars in our sample. Bright radio loud blazars with synchrotron peaks in their SEDs located below $10^{13.4}$ Hz have high-energy peaks that lie well below the lower energy cutoff of the LAT, resulting in a low gamma-ray flux. Future space telescopes such as *Astro-H* which cover the hard X-ray/soft gamma-ray regime below 100 MeV therefore offer great potential for detecting these blazars.

The authors thank Ken Kellermann for helpful discussions. The MOJAVE program is supported under NASA-Fermi grant NNX12A087G. MFA was supported by NASA-*Fermi* GI grants NNX09AU16G, NNX10AP16G and NNX11AO13G and NSF grant AST-0607523. TH

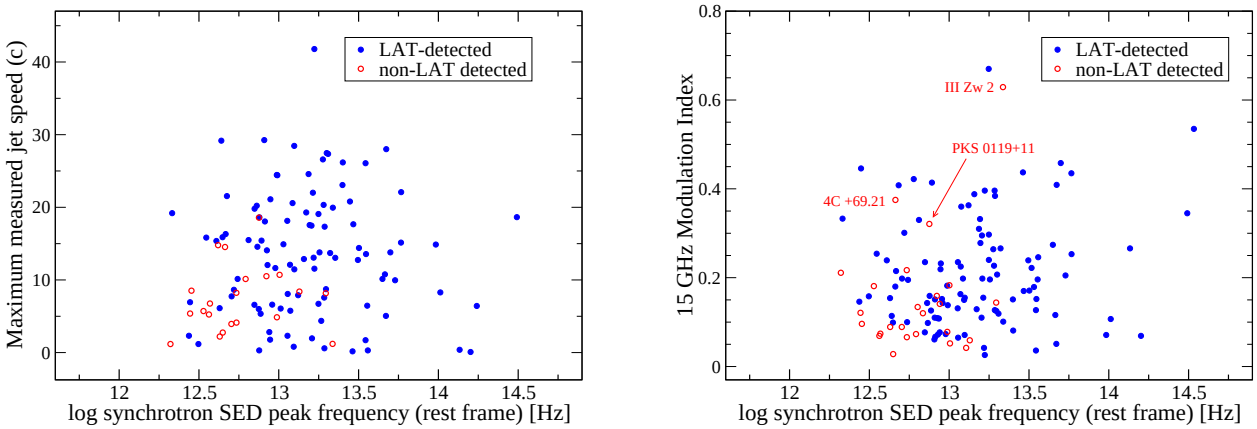

Figure 3. Left panel: plot of maximum measured jet speed versus rest frame synchrotron SED peak frequency. The blue filled circles represent LAT-detected AGN, while the open red circles represent non-LAT detected AGN. Right panel: same, but for 15 GHz OVRO modulation index.

was supported by the Academy of Finland project number 267324. The National Radio Astronomy Observatory is a facility of the National Science Foundation operated under cooperative agreement by Associated Universities, Inc. This work made use of the Swinburne University of Technology software correlator (Deller et al. 2011), developed as part of the Australian Major National Research Facilities Programme and operated under licence.

REFERENCES

Abdo, A. A., et al. 2009, ApJS, 183, 46
—. 2010a, ApJS, 188, 405
—. 2010b, ApJ, 720, 912
—. 2010c, ApJ, 722, 520
—. 2010d, ApJ, 715, 429
—. 2010e, ApJ, 716, 30
Acero, F., et al. 2015, ApJS, 218, 23
Ackermann, M., et al. 2011, ApJ, 741, 30
—. 2015, ArXiv e-prints, 1501.06054
Aller, M. F., Hughes, P. A., Aller, H. D., Latimer, G. E., & Hovatta, T. 2014, ApJ, 791, 53
Atwood, W. B., et al. 2009, ApJ, 697, 1071
Becker, R. H., White, R. L., & Helfand, D. J. 1995, ApJ, 450, 559
Carpenter, B., Ojha, R., D'Ammando, F., Orienti, M., & Cheung, C. C. 2014, The Astronomer's Telegram, 5838, 1
Condon, J. J., Cotton, W. D., Greisen, E. W., Yin, Q. F., Perley, R. A., Taylor, G. B., & Broderick, J. J. 1998, AJ, 115, 1693
Deller, A. T., et al. 2011, PASP, 123, 275
Dermer, C. D. 1995, ApJL, 446, L63
Dermer, C. D., & Schlickeiser, R. 1993, ApJ, 416, 458
Finke, J. D. 2013, ApJ, 763, 134
Fuhrmann, L., et al. 2014, MNRAS, 441, 1899
Giommi, P., et al. 2012, A&A, 541, A160
Gregory, P. C., Scott, W. K., Douglas, K., & Condon, J. J. 1996, ApJS, 103, 427
Hovatta, T., Valtaoja, E., Tornikoski, M., & Lähteenmäki, A. 2009, A&A, 498, 723
Jorstad, S. G., et al. 2005, AJ, 130, 1418
Kovalev, Y. Y., et al. 2009, ApJL, 696, L17
Lähteenmäki, A., & Valtaoja, E. 1999, ApJ, 521, 493
Lister, M. L. 2001, ApJ, 561, 676
Lister, M. L., Homan, D. C., Kadler, M., Kellermann, K. I., Kovalev, Y. Y., Ros, E., Savolainen, T., & Zensus, J. A. 2009a, ApJL, 696, L22
Lister, M. L., Tingay, S. J., & Preston, R. A. 2001, ApJ, 554, 964
Lister, M. L., et al. 2009b, AJ, 137, 3718
—. 2011, ApJ, 742, 27
—. 2013, AJ, 146, 120
Mahony, E. K., Sadler, E. M., Murphy, T., Ekers, R. D., Edwards, P. G., & Massardi, M. 2010, ApJ, 718, 587
Massaro, F., et al. 2015, ApJS, 217, 2
Mufakharov, T., Mingaliev, M., Sotnikova, Y., Naiden, Y., & Erkenov, A. 2015, MNRAS, 450, 2658
Murphy, T., et al. 2010, MNRAS, 402, 2403
Richards, J. L., Hovatta, T., Max-Moerbeck, W., Pavlidou, V., Pearson, T. J., & Readhead, A. C. S. 2014, MNRAS, 438, 3058
Richards, J. L., et al. 2011, ApJS, 194, 29
Savolainen, T., Homan, D. C., Hovatta, T., Kadler, M., Kovalev, Y. Y., Lister, M. L., Ros, E., & Zensus, J. A. 2010, A&A, 512, A24
Sikora, M., Begelman, M. C., & Rees, M. J. 1994, ApJ, 421, 153

Table 1
1.5 Jy MOJAVE AGN Sample Properties

J2000 (1)	Alias (2)	*Fermi* Catalog Name (3)	z (4)	$S_{\rm ext}$ (5)	$S_{\rm max}$ (6)	$S_{\rm med}$ (7)	a (8)	$\nu_{\rm p,obs}$ (9)	$\nu_{\rm p,rest}$ (10)
J0006−0623	NRAO 005	···	0.3467	0.08	2.69	2.09	0.78	13.0	13.1
J0010+1058	III Zw 2	···	0.0893	···	1.82	0.72	0.81	13.3	13.3
J0019+7327	S5 0016+73	···	1.781	···	1.48	1.10	0.66	12.3	12.7
J0050−0929	PKS 0048−09	3FGL J0050.6−0929	0.635	0.04	2.33	0.82	1.10	14.3	14.5
J0102+5824[a]	TXS 0059+581	3FGL J0102.8+5825	0.644	···	5.41	2.49	1.21	12.7	12.9
J0108+0135	4C +01.02	3FGL J0108.7+0134	2.099	0.14	4.27	3.38	1.28	12.5	13.0
J0112+2244	S2 0109+22	3FGL J0112.1+2245	0.265	···	1.36	0.37	0.90	13.4	13.5
J0112+3522	B2 0109+35	···	0.450	···	1.37	0.99	0.89	12.8	13.0
J0121+1149	PKS 0119+11	···	0.570	0.05	4.36	2.10	1.07	12.7	12.9
J0125−0005	UM 321	···	1.0765	0.07	1.07	0.89	0.66	···	···
J0132−1654	OC −150	3FGL J0132.6−1655	1.020	···	2.91	2.11	2.82	12.9	13.2
J0136+4751	DA 55	3FGL J0137.0+4752	0.859	···	4.90	3.31	0.86	12.3	12.6
J0204+1514	4C +15.05	3FGL J0205.0+1510	0.405	0.24	1.26	0.82	0.42	12.5	12.6
J0205+3212	B2 0202+31	3FGL J0204.8+3212	1.466	···	3.51	2.53	1.05	12.3	12.7
J0204−1701	PKS 0202−17	3FGL J0205.2−1700	1.739	0.12	1.46	1.31	1.03	12.5	12.9
J0217+7349	S5 0212+73	3FGL J0217.5+7349	2.367	0.04	3.96	3.23	0.98	12.3	12.8
J0217+0144	OD 026	3FGL J0217.8+0143	1.715	···	2.36	1.64	0.62	13.1	13.5
J0228+6721[a]	4C +67.05	···	0.523	0.02	1.37	0.88	0.57	12.8	13.0
J0231+1322	4C +13.14	···	2.059	0.07	2.06	1.68	1.37	12.3	12.8
J0237+2848	4C +28.07	3FGL J0237.9+2848	1.206	···	4.27	2.65	0.82	12.9	13.2
J0238+1636	AO 0235+164	3FGL J0238.6+1636	0.940	···	6.73	1.24	1.36	13.0	13.2
J0241−0815	NGC 1052	···	0.005037	0.10	1.63	1.11	0.66	···	···
J0244+6228[a]	TXS 0241+622	···	0.045	···	2.33	1.69	1.35	13.4	13.5
J0303+4716[a]	4C +47.08	3FGL J0303.6+4716	···	0.05	2.44	1.91	1.42	13.4	···
J0319+4130	3C 84	3FGL J0319.8+4130	0.0176	1.38	29.80	19.83	1.09	12.9	12.9
J0336+3218	NRAO 140	3FGL J0336.5+3210	1.259	···	3.12	2.51	1.12	13.0	13.4
J0339−0146	CTA 26	3FGL J0339.5−0146	0.852	···	3.85	2.53	1.12	12.7	13.0
J0359+5057[a]	NRAO 150	[b]	1.520	0.13	16.05	11.73	1.22	12.4	12.8
J0403+2600	CTD 026	···	2.109	···	2.16	1.90	1.37	12.3	12.8
J0405−1308	PKS 0403−13	3FGL J0405.5−1307	0.571	0.76	1.13	0.87	0.60	13.2	13.4
J0418+3801[a]	3C 111	3FGL J0418.5+3813c	0.0491	0.90	6.16	3.13	0.89	13.3	13.3
J0423−0120	PKS 0420−01	3FGL J0423.2−0119	0.9161	···	8.65	5.32	0.63	12.8	13.1
J0424+0036	PKS 0422+00	3FGL J0424.7+0035	0.268	···	1.03	0.57	0.50	14.0	14.1
J0433+0521	3C 120	[c]	0.033	0.39	3.54	2.08	0.63	13.5	13.6
J0442−0017	NRAO 190	3FGL J0442.6−0017	0.845	···	2.30	1.46	1.36	13.0	13.3
J0449+1121	PKS 0446+11	3FGL J0449.0+1121	2.153	···	1.74	1.07	0.69	12.8	13.2
J0453−2807	OF −285	3FGL J0453.2−2808	2.559	···	1.72	1.55	···	12.5	13.0
J0457−2324	PKS 0454−234	3FGL J0457.0−2324	1.003	···	2.39	1.83	1.01	12.7	13.0
J0501−0159	S3 0458−02	3FGL J0501.2−0157	2.286	0.07	1.52	1.12	0.51	13.0	13.5
J0530+1331	PKS 0528+134	3FGL J0530.8+1330	2.070	···	3.54	1.83	0.33	12.8	13.3
J0532+0732	OG 050	3FGL J0532.7+0732	1.254	0.06	1.65	1.35	0.94	12.6	12.9
J0533+4822[a]	TXS 0529+483	3FGL J0533.2+4822	1.160	0.03	1.64	1.30	0.82	13.1	13.4
J0541−0541	PKS 0539−057	1FGL J0540.9−0547	0.838	0.03	1.41	0.82	1.44	12.4	12.7
J0555+3948[a]	DA 193	···	2.363	0.21	4.21	3.85	0.74	···	···
J0607−0834	OC −010	3FGL J0608.0−0835	0.870	···	3.33	2.15	0.92	12.1	12.3
J0609−1542	PKS 0607−15	···	0.3226	···	5.99	3.64	0.52	12.2	12.3
J0646+4451	OH 471	···	3.396	···	3.81	3.35	0.86	11.8	12.5
J0650−1637[a]	PKS 0648−16	3FGL J0650.4−1636	···	0.16	2.63	1.83	0.69	···	···
J0721+7120	S5 0716+71	3FGL J0721.9+7120	0.127	0.04	4.12	1.87	1.14	14.4	14.5
J0725−0054[a]	PKS 0723−008	3FGL J0725.8−0054	0.127	0.05	4.55	4.12	2.19	13.4	13.5
J0730−1141[a]	PKS 0727−11	3FGL J0730.2−1141	1.591	···	9.54	6.86	1.34	12.6	13.0
J0733+5022	TXS 0730+504	3FGL J0733.8+5021	0.720	···	0.74	0.60	0.51	12.7	12.9
J0738+1742	OI 158	3FGL J0738.1+1741	0.450	0.08	0.92	0.59	0.46	13.5	13.7
J0739+0137	OI 061	3FGL J0739.4+0137	0.1894	0.03	2.41	1.21	0.75	13.2	13.3
J0741+3112	OI 363	···	0.631	0.05	1.78	1.20	0.58	···	···
J0745+1011	PKS B0742+103	···	2.624	0.04	1.47	1.38	0.73	···	···
J0745−0044	OI −072	···	0.996	···	1.55	1.37	0.80	···	···
J0748+2400	S3 0745+24	3FGL J0748.3+2401	0.4092	···	1.63	1.17	1.05	12.8	13.0
J0750+1231	OI 280	3FGL J0750.6+1232	0.889	···	5.04	4.06	1.11	12.6	12.9
J0757+0956	PKS 0754+100	3FGL J0757.0+0956	0.266	···	2.01	1.46	0.69	13.4	13.5
J0808+4950	OJ 508	3FGL J0807.9+4946	1.436	···	1.03	0.47	0.43	12.1	12.5
J0808−0751	PKS 0805−07	3FGL J0808.2−0751	1.837	0.03	2.53	1.52	1.53	12.8	13.2
J0811+0146	OJ 014	3FGL J0811.3+0146	1.148	···	1.36	0.97	0.86	13.0	13.3
J0818+4222	OJ 425	3FGL J0818.2+4223	···	···	2.12	1.55	1.17	13.1	···
J0824+3916	4C +39.23	3FGL J0824.9+3916	1.216	0.13	1.36	1.05	0.82	12.6	12.9
J0825+0309	PKS 0823+033	3FGL J0826.0+0307	0.505	···	2.14	0.76	1.02	13.0	13.2
J0830+2410	OJ 248	3FGL J0830.7+2408	0.942	···	2.08	1.31	0.94	12.6	12.8
J0831+0429	OJ 049	3FGL J0831.9+0430	0.174	···	1.20	0.66	0.70	13.6	13.6
J0836−2016	PKS 0834−20	3FGL J0836.5−2020	2.752	0.14	2.18	2.07	0.63	11.9	12.4
J0841+7053	4C +71.07	3FGL J0841.4+7053	2.218	0.02	3.07	2.19	1.16	12.4	12.9
J0840+1312	3C 207	3FGL J0840.8+1315	0.680	0.13	1.79	1.27	0.93	···	···
J0850−1213	PMN J0850−1213	3FGL J0850.2−1214	0.566	···	1.62	0.57	1.70	13.1	13.3
J0854+2006	OJ 287	3FGL J0854.8+2006	0.306	···	11.05	4.68	1.88	13.7	13.8
J0902−1415	PKS B0859−140	···	1.339	0.16	1.28	0.83	0.65	···	···

Table 1 — *Continued*

J2000 (1)	Alias (2)	*Fermi* Catalog Name (3)	z (4)	$S_{\rm ext}$ (5)	$S_{\rm max}$ (6)	$S_{\rm med}$ (7)	a (8)	$\nu_{\rm p,obs}$ (9)	$\nu_{\rm p,rest}$ (10)
J0909+0121	4C +01.24	3FGL J0909.1+0121	1.026	···	2.69	1.42	0.97	13.5	13.8
J0920+4441	S4 0917+44	3FGL J0920.9+4442	2.189	···	2.17	2.02	1.48	13.0	13.5
J0921+6215	OK 630	3FGL J0921.8+6215	1.453	0.04	1.45	1.20	0.75	12.5	12.9
J0927+3902	4C +39.25	···	0.695	···	12.33	10.39	0.89	12.4	12.6
J0948+4039	4C +40.24	3FGL J0948.6+4041	1.249	0.06	1.82	1.43	0.94	12.5	12.9
J0958+6533	S4 0954+65	3FGL J0958.6+6534	0.367	···	2.53	1.31	0.99	13.4	13.5
J0958+4725	OK 492	3FGL J0957.4+4728	1.882	···	1.20	0.75	0.63	12.2	12.6
J1033+4116	S4 1030+41	3FGL J1033.2+4116	1.117	···	2.71	1.39	···	12.8	13.1
J1037−2934	PKS 1034−293	3FGL J1037.0−2934	0.312	0.09	2.57	2.28	0.94	12.8	12.9
J1038+0512	PKS 1036+054	···	0.473	···	1.95	1.29	0.69	12.4	12.5
J1041+0610	4C +06.41	···	1.265	···	1.53	1.34	0.83	12.7	13.0
J1048−1909	PKS 1045−18	···	0.595	···	2.09	1.21	1.20	12.7	12.9
J1058+0133	4C +01.28	3FGL J1058.5+0133	0.888	0.08	5.51	4.77	0.91	12.8	13.1
J1127−1857	PKS 1124−186	3FGL J1127.0−1857	1.048	0.08	3.29	1.80	1.14	13.2	13.5
J1130−1449	PKS 1127−14	3FGL J1129.9−1446	1.184	0.04	3.71	2.29	0.94	12.7	13.0
J1130+3815	B2 1128+38	3FGL J1131.4+3819	1.733	0.03	1.52	1.23	0.98	12.3	12.7
J1153+4931	4C +49.22	3FGL J1153.4+4932	0.3334	0.04	1.93	1.78	1.76	13.1	13.2
J1153+8058	S5 1150+81	···	1.250	0.06	1.11	0.99	0.62	12.4	12.8
J1159+2914	4C +29.45	3FGL J1159.5+2914	0.725	0.10	3.60	2.26	0.64	12.9	13.2
J1215−1731	PKS 1213−17	···	···	0.05	1.95	1.70	0.75	···	···
J1222+0413	4C +04.42	3FGL J1222.4+0414	0.966	···	1.42	1.00	1.21	12.8	13.1
J1224+2122	4C +21.35	3FGL J1224.9+2122	0.434	0.16	2.56	1.99	1.05	13.1	13.3
J1229+0203	3C 273	3FGL J1229.1+0202	0.1583	5.07	27.60	22.97	0.63	13.9	14.0
J1230+1223	M87	3FGL J1230.9+1224	0.00436	24.07	4.62	2.13	1.02	···	···
J1256−0547	3C 279	3FGL J1256.1−0547	0.536	···	33.71	15.90	1.05	12.9	13.1
J1310+3220	OP 313	3FGL J1310.6+3222	0.997	···	3.06	2.70	0.77	13.0	13.3
J1327+2210	B2 1324+22	3FGL J1326.8+2211	1.403	···	1.46	1.03	0.64	12.5	12.9
J1337−1257	PKS 1335−127	3FGL J1337.6−1257	0.539	0.09	6.80	4.17	0.58	12.5	12.7
J1408−0752	PKS B1406−076	3FGL J1408.8−0751	1.494	···	1.10	0.95	0.69	12.7	13.1
J1415+1320	PKS B1413+135	3FGL J1416.0+1325	0.247	···	1.23	0.67	0.51	12.8	12.9
J1419+3821	B3 1417+385	3FGL J1419.8+3819	1.831	···	1.21	0.62	0.73	12.4	12.9
J1436+6336	VIPS 0792	···	2.066	0.07	1.54	1.43	1.09	12.6	13.1
J1459+7140	3C 309.1	···	0.904	0.80	0.80	0.61	0.41	···	···
J1504+1029	OR 103	3FGL J1504.4+1029	1.8385	···	3.33	1.51	1.22	12.7	13.2
J1507−1652	PKS 1504−167	···	0.876	0.04	1.04	0.86	0.45	12.4	12.7
J1512−0905	PKS 1510−08	3FGL J1512.8−0906	0.360	0.04	6.68	2.50	1.34	13.5	13.7
J1516+1932	PKS 1514+197	3FGL J1516.9+1926	1.070	···	1.75	1.02	1.71	12.9	13.2
J1517−2422	AP Librae	3FGL J1517.6−2422	0.049	···	2.58	2.12	0.75	14.2	14.2
J1522−2730	PKS 1519−273	3FGL J1522.6−2730	1.297	···	0.99	0.87	0.51	12.8	13.2
J1540+1447	4C +14.60	3FGL J1540.8+1449	0.606	0.12	1.18	0.92	0.83	13.1	13.3
J1549+0237	PKS 1546+027	3FGL J1549.4+0237	0.414	···	2.60	1.79	0.58	12.9	13.1
J1550+0527	4C +05.64	3FGL J1550.5+0526	1.417	0.07	3.04	2.74	0.93	12.8	13.2
J1608+1029	4C +10.45	3FGL J1608.6+1029	1.232	···	1.45	0.88	0.63	12.9	13.2
J1613+3412	DA 406	3FGL J1613.8+3410	1.40	···	3.76	2.57	0.66	12.3	12.6
J1625−2527	PKS 1622−253	3FGL J1625.7−2527	0.786	0.19	2.91	2.00	0.67	12.6	12.9
J1626−2951	PKS 1622−29	3FGL J1626.0−2951	0.815	···	2.38	1.46	0.61	12.6	12.9
J1635+3808	4C +38.41	3FGL J1635.2+3809	1.813	···	4.15	3.37	0.93	12.5	12.9
J1638+5720	OS 562	3FGL J1637.9+5719	0.751	0.04	2.33	1.46	0.89	···	···
J1640+3946	NRAO 512	3FGL J1640.6+3945	1.666	···	1.85	1.09	1.08	12.1	12.5
J1642+3948	3C 345	3FGL J1642.9+3950	0.593	0.30	9.15	7.36	0.74	13.0	13.2
J1642+6856	4C +69.21	···	0.751	···	4.73	2.46	2.17	12.4	12.7
J1658+0741	PKS 1655+077	···	0.621	0.04	2.10	1.88	0.94	12.4	12.6
J1727+4530	S4 1726+45	3FGL J1727.1+4531	0.717	···	2.49	1.27	1.14	12.8	13.1
J1733−1304	NRAO 530	3FGL J1733.0−1305	0.902	0.46	5.26	4.26	0.35	13.0	13.3
J1740+5211	4C +51.37	3FGL J1740.3+5211	1.379	···	2.00	1.27	0.75	13.1	13.5
J1743−0350	PKS 1741−03	3FGL J1744.3−0353	1.054	···	5.66	3.72	0.72	12.3	12.7
J1751+0939	4C +09.57	3FGL J1751.5+0939	0.322	···	7.37	4.38	0.84	13.0	13.1
J1753+2848	B2 1751+28	···	1.118	···	1.88	1.07	0.94	···	···
J1800+3848	B3 1758+388B	···	2.092	···	1.29	1.06	0.72	12.1	12.6
J1801+4404	S4 1800+44	3FGL J1801.5+4403	0.663	0.05	1.46	0.96	0.84	12.6	12.8
J1800+7828	S5 1803+784	3FGL J1800.5+7827	0.6797	0.02	3.40	2.65	1.04	13.4	13.7
J1806+6949	3C 371	3FGL J1806.7+6949	0.051	0.23	1.64	1.34	0.95	14.2	14.2
J1824+5651	4C +56.27	3FGL J1824.2+5649	0.664	0.09	1.67	1.50	0.64	13.2	13.4
J1829+4844	3C 380	3FGL J1829.6+4844	0.692	1.12	2.56	2.10	0.96	13.0	13.2
J1842+6809	S4 1842+68	3FGL J1842.8+6810	0.472	0.02	1.64	0.60	0.92	12.3	12.4
J1849+6705	S4 1849+67	3FGL J1849.2+6705	0.657	···	3.13	2.44	1.03	13.2	13.4
J1911−2006	PKS B1908−201	3FGL J1911.2−2006	1.119	···	3.66	1.65	1.29	12.9	13.3
J1923−2104	OV −235	3FGL J1923.5−2104	0.874	···	2.07	1.75	1.09	···	···
J1924−2914	PKS B1921−293	3FGL J1924.8−2914	0.3526	1.39	20.99	13.40	0.86	12.5	12.6
J1925+2106[a]	PKS B1923+210	···	···	0.05	2.33	1.82	0.70	12.2	···
J1927+7358	4C +73.18	···	0.302	0.03	4.59	4.05	1.02	13.2	13.3
J1939−1525	PKS 1936−15	···	1.657	0.03	0.88	0.69	0.50	12.0	12.4
J1959+4044[a]	Cygnus A	···	0.0561	66.10	29.01	1.11	1.01	···	···
J2000−1748	PKS 1958−179	3FGL J2001.0−1750	0.652	···	3.29	1.26	1.16	12.6	12.8
J2007+4029[a]	TXS 2005+403	···	1.736	···	3.88	3.49	1.25	12.2	12.6
J2005+7752	S5 2007+77	3FGL J2005.2+7752	0.342	0.08	1.55	0.80	0.83	13.4	13.6

Table 1 — *Continued*

J2000 (1)	Alias (2)	*Fermi* Catalog Name (3)	z (4)	$S_{\rm ext}$ (5)	$S_{\rm max}$ (6)	$S_{\rm med}$ (7)	a (8)	$\nu_{\rm p,obs}$ (9)	$\nu_{\rm p,rest}$ (10)
J2011−1546	PKS 2008−159	···	1.180	···	2.48	2.15	1.01	12.7	13.0
J2015+3710[a]	TXS 2013+370	3FGL J2015.6+3709	0.859	0.16	4.42	2.95	0.99	···	···
J2023+3153[a]	4C +31.56	3FGL J2023.2+3154	0.356	0.14	1.27	1.19	0.59	···	···
J2022+6136	OW 637	···	0.227	···	2.41	2.32	0.75	···	···
J2025+3343[a]	B2 2023+33	3FGL J2025.2+3340	0.219	···	6.42	3.71	1.95	···	···
J2031+1219	PKS 2029+121	3FGL J2031.8+1223	1.213	···	2.10	1.51	1.53	12.6	13.0
J2038+5119[a]	3C 418	3FGL J2038.8+5113	1.686	0.30	3.43	3.12	1.24	12.5	12.9
J2123+0535	OX 036	3FGL J2123.6+0533	1.941	···	1.99	1.64	0.53	12.5	13.0
J2131−1207	PKS 2128−12	···	0.501	0.12	2.22	1.81	0.67	···	···
J2134−0153	4C −02.81	3FGL J2134.1−0152	1.284	···	2.72	2.25	1.02	13.0	13.3
J2136+0041	PKS 2134+004	···	1.932	···	7.32	6.86	0.99	···	···
J2139+1423	OX 161	···	2.427	···	2.95	2.63	1.03	12.2	12.7
J2148+0657	4C +06.69	1FGL J2148.5+0654	0.999	0.04	5.90	5.39	0.52	12.6	12.9
J2158−1501	PKS 2155−152	3FGL J2158.0−1501	0.672	···	3.99	1.88	1.52	12.8	13.1
J2202+4216	BL Lac	3FGL J2202.7+4217	0.0686	0.02	7.83	4.40	1.24	13.7	13.7
J2203+1725	PKS 2201+171	3FGL J2203.4+1725	1.076	···	1.66	1.15	0.83	13.2	13.5
J2203+3145	4C +31.63	3FGL J2203.7+3143	0.2947	···	3.54	2.90	0.94	13.9	14.0
J2212+2355	PKS 2209+236	3FGL J2212.0+2355	1.125	···	1.28	0.91	0.67	12.1	12.4
J2218−0335	PKS 2216−03	···	0.901	0.11	2.04	1.51	0.60	12.3	12.6
J2225+2118	DA 580	···	1.959	0.09	1.91	1.37	1.54	12.5	12.9
J2225−0457	3C 446	3FGL J2225.8−0454	1.404	0.88	8.05	5.86	1.01	12.9	13.3
J2229−0832	PHL 5225	3FGL J2229.7−0833	1.5595	···	3.80	2.39	1.76	12.8	13.2
J2232+1143	CTA 102	3FGL J2232.5+1143	1.037	0.14	5.91	3.45	0.90	12.4	12.7
J2236+2828	CTD 135	3FGL J2236.3+2829	0.790	···	1.53	1.19	1.04	12.9	13.2
J2246−1206	PKS 2243−123	···	0.632	···	2.75	2.33	0.79	12.3	12.6
J2253+1608	3C 454.3	3FGL J2254.0+1608	0.859	···	28.12	13.10	1.50	13.4	13.7
J2258−2758	PKS 2255−282	3FGL J2258.0−2759	0.927	···	4.72	3.13	0.51	12.6	12.9
J2327+0940	OZ 042	3FGL J2327.7+0941	1.841	···	2.82	1.37	1.25	12.2	12.7
J2334+0736	TXS 2331+073	3FGL J2334.1+0732	0.401	···	1.54	1.07	1.01	12.7	12.9
J2348−1631	PKS 2345−16	3FGL J2348.0−1630	0.576	···	2.48	1.96	0.85	12.9	13.1
J2354+4553	4C +45.51	3FGL J2354.1+4605	1.986	0.15	1.01	0.81	0.44	12.2	12.7

Note. — Columns are as follows: (1) J2000 name, (2) other name, (3) Fermi catalog name, (4) redshift, (5) arcsecond-scale flux density at 15 GHz in Jy, (6) maximum 15 GHz VLBA flux density in Jy during 3FGL time window, (7) median 15 GHz VLBA flux density in Jy during 3FGL time window, (8) radio activity index, (9) log of observed synchrotron peak frequency in Hz (observer frame), (10) log of observed synchrotron peak frequency in Hz (rest frame).

[a] Low galactic latitude ($|b| < 10°$)

[b] *Fermi* LAT detection reported by Carpenter et al. (2014)

[c] *Fermi* LAT detection reported by Abdo et al. (2010b)

Table 2
Statistical Tests on LAT and Non-LAT Sub-samples

Property	Kolmogorov-Smirnov	Wilcoxon Rank Sum
Synchrotron peak location (observed)	1×10^{-4}	3×10^{-5}
Synchrotron peak location (rest frame)	1×10^{-4}	1×10^{-5}
Maximum observed jet speed	2×10^{-6}	3×10^{-5}
15 GHz modulation index	5×10^{-4}	9×10^{-5}
Redshift	0.50	0.45
Radio activity index[a]	0.10	0.14
Median VLBA radio flux density[a]	0.86	0.50
Maximum VLBA radio flux density[a]	0.04	0.05
Median VLBA radio luminosity[a]	0.86	0.80
Maximum VLBA radio luminosity[a]	0.76	0.73

Note. — The tabulated values indicate the probability of obtaining the observed distributions in the LAT and non-LAT detected subsamples, under the null hypothesis that they came from the same parent distribution.

[a] During the 3FGL time window.